Available online at www.sciencedirect.com
ScienceDirect
Trans. Nonferrous Met. Soc. China 31(2021) 391−403
Transactions of Nonferrous Metals Society of China
www.tnmsc.cn

Effect of cooling rate on solidification microstructure and mechanical properties of TiB_2-containing TiAl alloy

Yi JIA[1,2,3], Zhi-dong LIU[1], Sha LI[1,2,3], Hao-ming YAO[1,2,3], Zhong-kai REN[1,2,3], Tao WANG[4], Jian-chao HAN[1,2,3], Shu-long XIAO[4], Yu-yong CHEN[4]

1. College of Mechanical and Vehicle Engineering, Taiyuan University of Technology, Taiyuan 030024, China;
2. Advanced Metal Composite Forming Technology and Equipment Engineering Research Center of Ministry of Education, Taiyuan University of Technology, Taiyuan 030024, China;
3. TYUT-UOW Joint Research Centre, Taiyuan University of Technology, Taiyuan 030024, China;
4. National Key Laboratory for Precision Hot Processing of Metals, Harbin Institute of Technology, Harbin 150001, China

Received 24 March 2020; accepted 1 December 2020

Abstract: Effects of cooling rate and 0.25 at.% TiB_2 addition on solidification microstructure and mechanical properties of Ti−48Al−2Cr−2Nb alloys fabricated by the investment casting with different thicknesses were studied. The results show that with the cooling rate increasing from 37 to 2×10^2 K/s, the solidification path of the studied alloys is unchanged. The grain size of the matrix alloy is refined from 650 to 300 μm, while the grain size of Ti−48Al−2Cr−2Nb−TiB_2 is reduced from 550 to 80 μm. The lamellar spacing of matrix alloy is reduced from 360 to 30 nm with increasing the cooling rate from 37 to 2×10^2 K/s, while TiB_2 addition shows little refinement effect on the lamellar spacing. Ti−48Al−2Cr−2Nb−TiB_2 sample under medium cooling rate (69 K/s) exhibits superior microhardness (HV 550) and ultimate tensile strength (570 MPa) among the studied alloys. The refined grain size, lamellar spacing and fine TiB_2 particles could account for the favorable mechanical properties of the studied TiB_2-containing alloy. The microstructure evolution was discussed in light of cooling rate, constitutional supercooling and borides addition.
Key words: titanium aluminides; TiB_2; cooling rate; microstructure evolution; mechanical properties

1 Introduction

Compared with titanium alloy and nickel-based alloy, TiAl-based alloy exhibits the characteristics of low density, high specific strength and specific rigidity, excellent oxidation resistance and creep resistance in the temperature range of 600−900 °C, and becomes the promising candidate material in the aviation field [1,2]. Because of poor deformability and narrow hot working window, investment casting has become the main forming method for the engineering application of TiAl alloy [3,4]. However, the unstable solidification condition during the casting process, coarse as-cast microstructure, and poor mechanical properties appear to be the key factors limiting the further application of this alloy [5,6].

Microalloying is one of the effective methods to refine the as-cast microstructure of TiAl alloy, such as adding B, C, Y and other elements. Boron was reported to be the most effective alloying element for grain refinement in the cast TiAl alloy, which can effectively refine the coarse columnar crystals and eliminate the microstructure anisotropy [7]. The refining effect of boron is affected by the solidification path and other alloying elements. There exists a threshold value of

Corresponding author: Jian-chao HAN, E-mail: hanjianchao@tyut.edu.cn; Tao WANG, E-mail: tyutwt@163.com
DOI: 10.1016/S1003-6326(21)65504-8

boron content for grain refinement [8]. For the peritectic TiAl alloy with high Al content, the threshold is reported as 0.5 at.%, while for the β-solidified TiAl with low Al content, the threshold is generally considered to be 0.2 at.% [9]. Meanwhile, the influence of B on the lamellar spacing appeared to be controversial. SRIVASTAVA et al [10] found that the lamellar spacing of the B-doped TiAl alloys was coarser than that in the B-free alloys under the same cooling condition. While MAZIASZ and LIU [11] observed that trace boron addition of 1.40×10^{-4} could refine the lamellar spacing. The influence of boron addition on the lamellar spacing of TiAl alloy was still inconclusive. Furthermore, WU and HWANG [12,13] found that the average grain size of TiAl alloy could be refined from 100 to 45 μm with 0.33 at.% Y addition. Meanwhile, some studies showed that the synergetic addition of Y and B can further refine the grain size and lamellar spacing [14]. LI et al [15,16] found that the microstructure refinement could be attributed to the significant constitutional supercooling at the solid−liquid interface induced by Y element. Similar to element B and Y, C alloying was reported to refine the grain size and lamellar spacing of TiAl alloy, accompanied by the precipitation of primary Ti_2AlC [17]. Research by WU et al [18] showed that trace C addition exhibited little influence on the grain size of Ti−46Al−8Nb alloy. While when the carbon content was increased to 1.4 at.%, the as-cast microstructure transformed from coarse columnar crystals into fine crystals with an average grain size of 40 μm. The influence of B, Y and C addition on the grain size and lamellar spacing of Ti−43Al−5Nb was compared by CUI et al [19], and it was found that the refinement effects could be arranged as B>Y>C and Y>C>B, respectively.

For the precision casting of TiAl alloy, most castings are thin-walled with complex shape and the wall thickness is often uneven. Therefore, the corresponding solidification process should be multifarious and will affect the final microstructure and mechanical property. However, most of the above researches were mainly focused on the single solidification state, which was difficult to reflect the actual production process. Therefore, for the typical cast TiAl alloy (Ti−48Al−2Cr−2Nb), 0.25 at.% TiB_2 is selected for microalloying. The effects of cooling rate (different wall thicknesses) on the solidification microstructure and mechanical properties are studied to provide a reference for the casting and engineering application of TiAl alloy.

2 Experiment and simulation

2.1 Test materials and methods

Alloys with nominal compositions of Ti−48Al−2Cr−2Nb and Ti−48Al−2Cr−2Nb−0.25TiB_2 (hereafter abbreviated as T4822 and T4822−TiB_2, at.%) were chosen for the investigation. The raw materials used in this study were sponge titanium (99.9 wt.%), high-purity Al ingot (99.99 wt.%), master alloy Al−56.8wt.%Nb, high-purity Cr (99.9 wt.%) and high-purity TiB_2 powder. The button ingots with a mass of 35 g were prepared by the vacuum non-consumable tungsten arc melting under an Ar atmosphere (pressure of ~50 kPa). In order to ensure the sufficient uniformity of composition and microstructure, electromagnetic stirring was conducted for 15 s during the melting process and each ingot was remelted 4−6 times. The button ingot was mechanically ground to remove the surface layer and then was remelted and cast after ultrasonic cleaning with anhydrous ethanol for 2 min.

Different cooling rates were obtained by the stepped plates with different thicknesses. The stepped plates were designed with a length of 30 mm, a width of 12 mm and a thickness of 1, 2 and 4 mm, respectively. The surface coating of mould was made of yttria, and the refractory material was ZrO_2 sand with different sizes. The ceramic mould was roasted and dewaxed at 900 °C for 2 h and cooled within the furnace. The pouring of the stepped plates was conducted on the LZ5 centrifugal titanium casting machine with the rotational speed of 700 r/min, and the melting and pouring processes were carried out under the protective Ar atmosphere (pressure of ~50 kPa). The ceramic mould was clamped with the special clamp made of stainless steel at room temperature. The pouring temperature was 1650 °C tested by the infrared thermometer. The castings were homogenized in a vacuum furnace at 900 °C for 5 h. The preparation process of the stepped plates is shown in Fig. 1. Areas A, B, and C represented the area with different thickness, respectively.

Fig. 1 Preparation of stepped plates

Microstructure observation samples were cut from the stepped plates by wire electrical discharge cutting. In order to avoid macro-segregation, the samples for analysis were all taken from the same position. Inductively coupled plasma-optical emission spectroscopy (ICP-OES) was used to analyze the chemical composition, and the results are listed in Table 1. The samples were observed by the scanning electron microscope (SEM) and transmission electron microscope (TEM). SEM observation sample was observed after electro-polishing. The electrolyte for electro-polishing was 60% methanol + 34% *n*-butanol + 6% perchloric acid, and the polishing temperature was −25 °C. The borides were observed after etching with HF acid for 20 s. TEM foils were prepared by twin-jet electro-polishing. The electrolyte and parameters were the same as those in electro-polishing. The grain size was calculated by the line intercept method according to GB T6394—2002. In order to obtain a reasonable average value, 3−5 view fields were randomly selected for measurement, and the average grain size was calculated finally. The lamellar spacing was determined using several bright-field TEM images in the "edge-on" condition.

Table 1 Chemical compositions of T4822 and T4822−TiB_2 alloys in different areas (at.%)

Alloy	Area	Al	Cr	Nb	Ti
T4822	A	47.76	1.88	1.93	Bal.
T4822	B	47.83	1.92	1.89	Bal.
T4822	C	47.85	1.96	1.88	Bal.
T4822−TiB_2	A	47.71	1.89	1.89	Bal.
T4822−TiB_2	B	47.92	1.92	1.95	Bal.
T4822−TiB_2	C	47.88	1.91	1.95	Bal.

Microhardness was measured by the HVS−5 Vickers hardness testing machine with a load of 0.98 N and load holding time of 15 s. Each sample was tested five times to obtain the average value. Flat tensile specimens with dimensions shown in Fig. 2 were tested on the Instron 5569 universal testing machine with the tensile strain rate of 4.2×10^{-4} s^{-1}. At least three tests were performed under each condition and average values were reported. The tensile fracture was observed to analyze the fracture behavior.

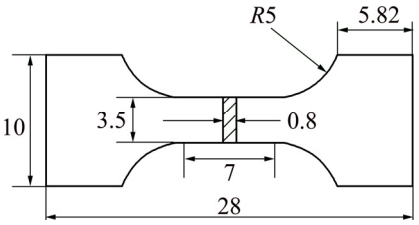

Fig. 2 Dimensions of tensile specimen (Unit: mm)

2.2 Casting process simulation

According to the literature and classical casting forming theory [20], the pouring and solidification process of the stepped plate were simulated by the ProCAST software. The thermophysical parameters used in the simulation are listed in Table 2, and the heat transfer coefficient was selected to be 500 $W\cdot m^{-2}\cdot K^{-1}$, referred to previous researches [21−23]. Figure 3 shows the temperature field distribution, predicted shrinkage porosity and temperature variation curves of the stepped casting during the casting process simulated by the ProCAST software. As shown in Fig. 3(b), the casting quality of the stepped plates was satisfactory and the porosity was mainly distributed in the pouring gate position. The inserted sections in Fig. 3(a) represented the selected positions for microstructure observation

Table 2 Thermophysical properties of TiAl alloy and zirconia mould

Thermophysical property	T4822	Mould (ZrO_2)
Density/($kg\cdot m^{-3}$)	3636	5680
Specific heat capacity/($J\cdot kg^{-1}\cdot K^{-1}$)	727	455
Thermal conductivity/($W\cdot m^{-1}\cdot K^{-1}$)	13.2	2.09
Liquidus temperature/°C	1525	−
Solidus temperature/°C	1450	−
Environment temperature/°C	25	25

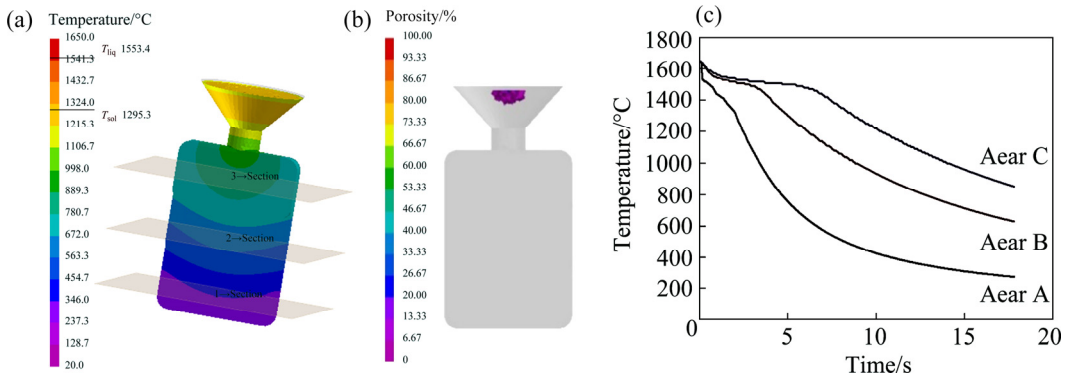

Fig. 3 Simulation results of TiAl stepped casting: (a) Temperature field distribution; (b) Predicted shrinkage porosity; (c) Temperature variation curves of three areas

and temperature simulation. The filling time of the stepped plates in this experiment was calculated to be 0.178 s, and the cooling rates from pouring temperature to the solidus temperature of Areas A, B and C were 2×10^2, 69 and 37 K/s, respectively.

3 Results and discussion

3.1 Effect of cooling rate on microstructure

Figure 4 shows the microstructure in different areas of the stepped plate casting. As shown, Ti−48Al−2Cr−2Nb alloy exhibits an obvious cubic-symmetric dendritic microstructure with dark and bright contrasts in Area A. Bright *B*2 phase can be clearly observed in the dendrites, which is reported as the sign of beta-to-alpha transformation [24]. The interdendritic regions with black contrast are demonstrated to be enriched with Al element. At the same time, it is noticed that there is no obvious growth direction for dendrites, which should be related to the lateral heat dissipation for the thin plate during the centrifugal casting process. From the high magnification image, the bright *B*2 phase and gray massive γ phase at grain boundary can be observed, and the difference of lamella orientation for the adjacent grains is relatively large. With the decrease of cooling rate, the microstructures in Areas B and C appear to be coarser, and bright β segregation and black Al segregation maintain as well in Figs. 4(b, c). This means that the primary phases of the matrix alloy solidified from melt in three different areas (A, B and C) are all β phases, following the solidification path as $L\rightarrow L+\beta\rightarrow L+\alpha\rightarrow\alpha\rightarrow\alpha+\gamma$ [25]. This further indicates that the solidification path of the matrix alloy is insensitive to the cooling rate.

Similar to the matrix alloy, T4822−TiB_2 alloy in Area A shows the fine equiaxed dendritic structure, and strip borides are mainly distributed in the interdendritic region. According to the high magnification image, it can be found that the interdendritic region consists of borides and fine blocky γ phases, accompanied by the isolated fine *B*2 blocks. Areas B and C show the similar microstructure, consisting of fine equiaxed grains. Borides are mainly observed along grain boundaries, and small amounts of borides are distributed within the lamellar colonies. Bright *B*2 phase remains inside the lamellar colony, while the volume fraction appears to be relatively small compared with that of Area A. This may be due to the sufficient diffusion time for β stabilizing elements during the peritectic transformation, thus leaving less residual high-temperature β phase in the as-cast microstructure.

Figure 5 shows the TEM morphology in Area A of T4822 alloy. Blocky γ and *B*2 phases can be observed along the boundary of lamellar colonies, and there is no special orientation relationship between the two phases. At the same time, it is noticed that the orientation angle between the adjacent lamellar colonies is close to 90°, and the contrast difference is significant. This indicates that the two lamellar colonies are transformed from different parent α phases.

Figure 6 shows the statistical results of the grain size in different areas of the stepped plate castings. As shown, the grain size of the two alloys gradually decreases with the increase of cooling rate. The matrix alloy and T4822−TiB_2 alloy in Area A show the smallest grain size of 300 and 80 μm, respectively. While the grain sizes of the two

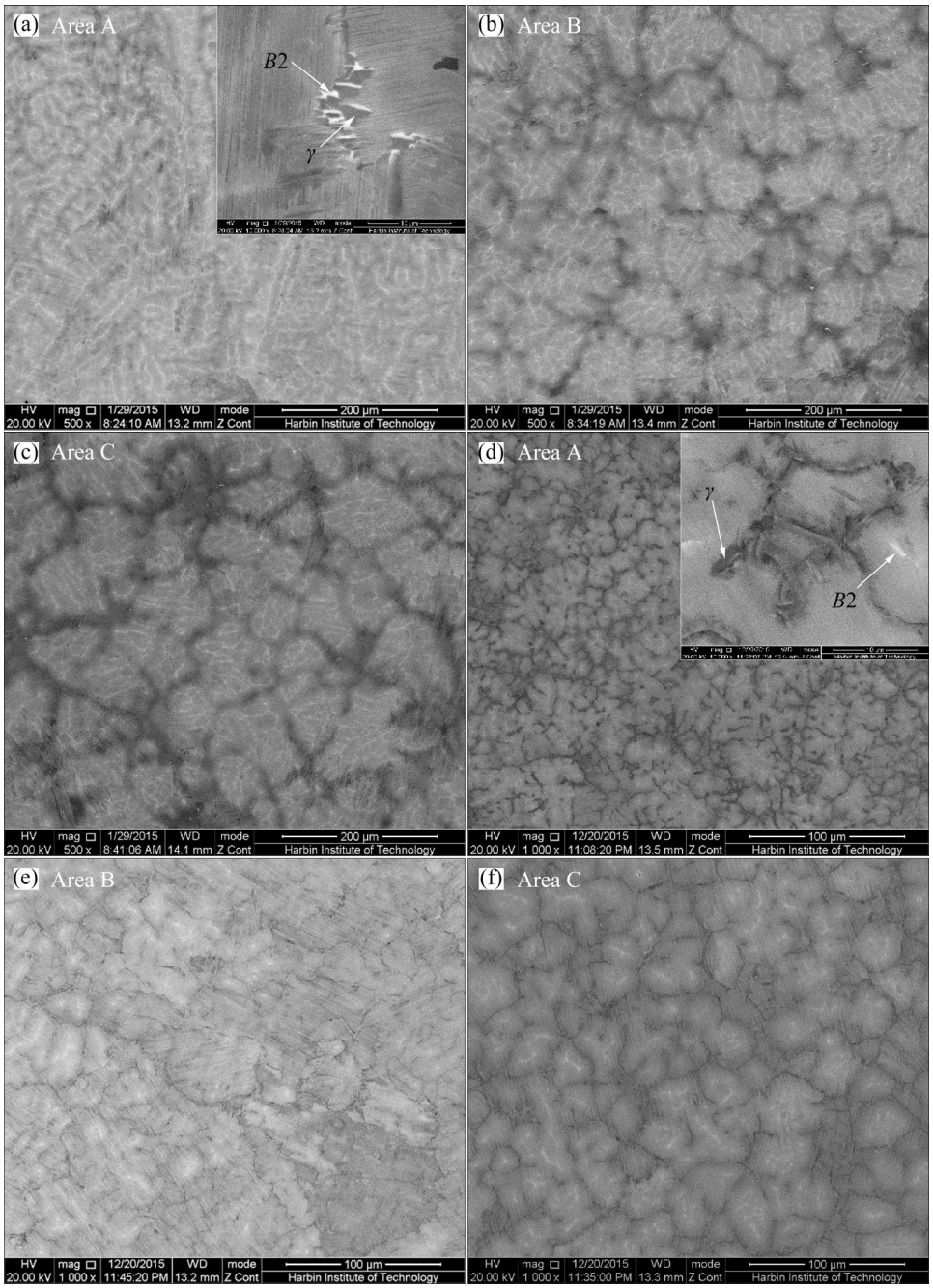

Fig. 4 SEM images of stepped plates with different cooling rates: (a−c) T4822; (d−f) T4822−TiB_2

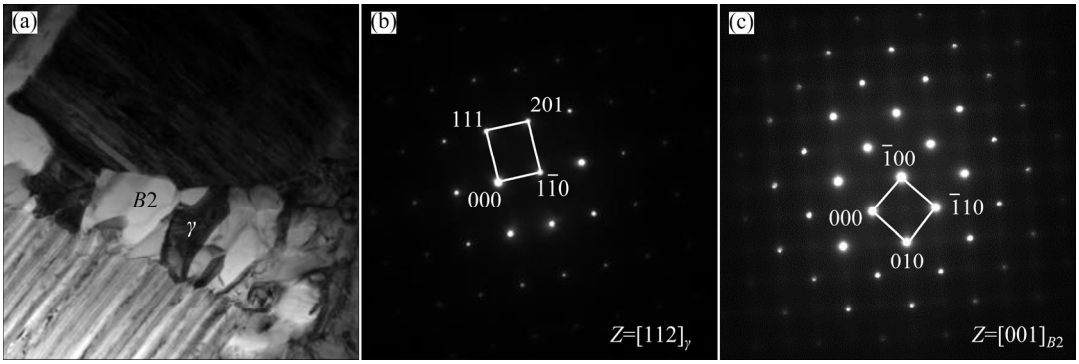

Fig. 5 TEM images of Area A in as-cast T4822 alloy: (a) Bright field image; (b, c) Corresponding selected area electron diffraction patterns

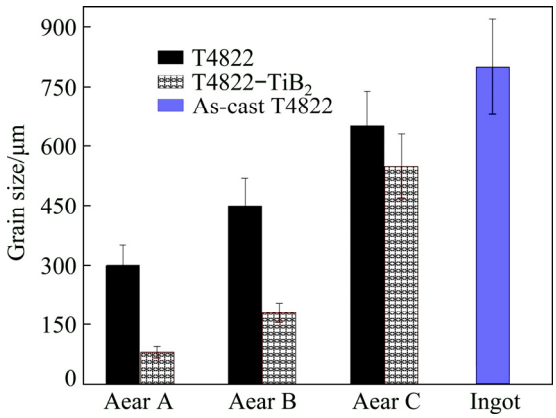

Fig. 6 Grain size statistical results of different stepped samples

alloys in Area C increase to 650 and 550 μm, respectively, which are still smaller than the grain size of the original ingot (800 μm) [26]. According to the above analysis, the solidification path of the two alloys maintains unchanged with different cooling rates. Therefore, for the matrix alloy, the grain refinement appears mainly due to the increased supercooling of the melt caused by the higher cooling rate. This can effectively improve the nucleation rate of the melt, promoting the microstructure refinement reasonably. For T4822−TiB_2 alloy, the grain refinement should be attributed to the effect of rapid cooling and boron element. In addition, it is worth noting that the grain size of T4822−TiB_2 alloy in Area C coarsens significantly, which is close to that of the matrix alloy. This indicates that the grain size of TiB_2-containing alloy appears more sensitive to the cooling rate under the action of TiB_2.

Figure 7 shows boride morphology in different areas of the T4822−TiB_2 stepped plate. As shown, borides in the three areas exhibit a multi-layer morphology composed of nano-scale lamellae parallel to the main plane. With the cooling rate of 2×10^2 K/s, the flaky boride is uniform in size with an average size of 3−5 μm, as shown in Fig. 7(a). While when the cooling rate decreases, the borides become coarse and present the curved shape with a larger width-to-thickness ratio, as shown in Figs. 7(b, c). The boride is broken in Fig. 7(c), which may result from the sample handling, indicating the unsubstantial state.

According to the binary phase diagram of Ti−Al alloy [25,27] and the composition of the residual room temperature *B*2 phase, it is deduced

Fig. 7 Morphologies of borides in different areas of T4822−TiB_2 stepped samples: (a) Area A; (b) Area B; (c) Area C

that the primary phases solidified from the liquid phase of the two alloys are β phases. During subsequent cooling, the primary β phase ultimately transforms to $\alpha_2+\gamma$ dual-phase through the following solidification path:

$$L+\beta\rightarrow L+\alpha\rightarrow\alpha\rightarrow\alpha+\gamma\rightarrow\alpha_2+\gamma$$

According to the phase diagram of the Ti−Al−B ternary alloy [28], the flaky boride with

the multi-layer structure in the present work should be the product of eutectic reaction of $L\rightarrow\beta+TiB_2$. The primary β phase can act as the nucleation site of TiB_2, and transforms to room temperature $B2$ phase through $\beta\rightarrow B2$ ordered transformation during the subsequent cooling process. Similarly, for the titanium alloy with special molar ratio of Ti/Fe, the ultrafine lamellar structure containing ultrafine bcc β-Ti and bcc $B2$ superstructured Ti(Fe,Co) lamellae is observed. The lamellar structure was reported as the similar product of eutectic reaction during the semi-solid sintering process [29,30]. Meanwhile, β stabilizing elements (Cr, Nb) can improve the stability of β phase and promote the residue of $B2$ phase in the layered borides at room temperature. However, due to high cooling rate, the temperature range for solidification and the precipitation of eutectic boride is narrow [28]. Both the β phase and TiB_2 phase exhibit a larger nucleation rate and shorter growth time, so the boride size appears to be small. With a slower cooling rate, the boride precipitated has a relatively long growth time, finally leading to the coarse borides with a large width-to-thickness ratio, as shown in Fig. 7(c).

It is worth noting that the cooling rate affects the grain refinement of TiAl-TiB_2 alloy. In the previous study of TiB_2-containing TiAl [6], the upper region of the ingot exhibited a coarse columnar microstructure (610 μm) while the bottom region had fine equiaxed microstructure (200 μm). CHENG [8] found that the refining effect of B on TiAl alloy was related to B content and other alloying elements (especially elements that promote boride precipitation, such as Ta). When B content was near the threshold, whether microstructure refinement occurred was closely related to the cooling rate during solidification. This could be mainly attributed to the constitutional supercooling.

The solid solubilities of element B in the liquid and solid phase of TiAl alloy are different, and the diffusion ability in liquid phase is limited. Meanwhile, the diffusion coefficient of Al element in liquid phase can be influenced by B addition. The above factors may induce the considerable constitutional supercooling at the solidification front of TiAl alloy melt [8,31]. With low TiB_2 addition, the B atoms are rejected to the solidification front and can be easily diffused into the liquid phase. This makes it difficult to form sufficient constitutional supercooling for grain refinement. When the content of TiB_2 exceeds the certain threshold, enough B atoms at the solidification front may lead to the enhanced constitutional supercooling at the solid−liquid interface. This additional driving force makes it easier for the nucleation of the β phase from the melt, promoting the nucleation rate of β phase. This can effectively refine the β dendrites during solidification. According to the solidification theory of TiAl alloy, during the subsequent peritectic reaction of $L+\beta\rightarrow\alpha$, α phase will nucleate on the interface between β phase and the liquid following the Burgers orientation relationship [32]. In addition, the flaky TiB_2 coupled with β phase will provide additional nucleation sites for α phase and eventually contribute to the refined as-cast microstructure. According to the constitutional supercooling conditions [33], when the cooling rate increases or the temperature gradient decreases, the nucleation of β grains can be promoted; otherwise, the nucleation can be inhibited. Therefore, the grain size of Area A is smaller than that of Areas B and C. It should be noted that compared with the grain size of Areas A and B and the literature of TiB_2/B-refined TiAl alloy [7,34], the grain size of Area C is much coarser but still smaller than that of matrix alloy. This should result from the assistance of borides on the nucleation. Therefore, the effect of TiB_2 on the microstructure refinement of T4822 in the present work should be the result of the combined effect of cooling rate and B element, and the slower cooling rate may inhibit the grain refinement. This is also consistent with the observation of GODFREY and LORETTO [35] and CHENG [8] that a large amount of B addition under extremely slow solidification conditions exhibited little influence on the cast microstructure of TiAl alloy.

Figure 8 shows the typical lamellar microstructure and the lamellar spacing statistical results of the studied alloys. The Area C of T4822 and T4822−TiB_2 alloy shows the coarse lamellar spacing of 360 and 350 nm, respectively, less than that of the matrix alloy ingot (450 nm). With the increase of cooling rate, the lamellar spacing of the two alloys decreases observably. In Area A, the matrix alloy exhibits the ultra-fine microstructure with lamellar spacing of 30 nm, almost one magnitude smaller than that of the ingot. It should be note that unlike grain size, the influence of TiB_2

on the lamellar spacing appears little. The lamellar spacing of T4822−TiB_2 alloy appears to be a little smaller compared with that of the matrix alloy with different cooling rates, as shown in Fig. 8(b).

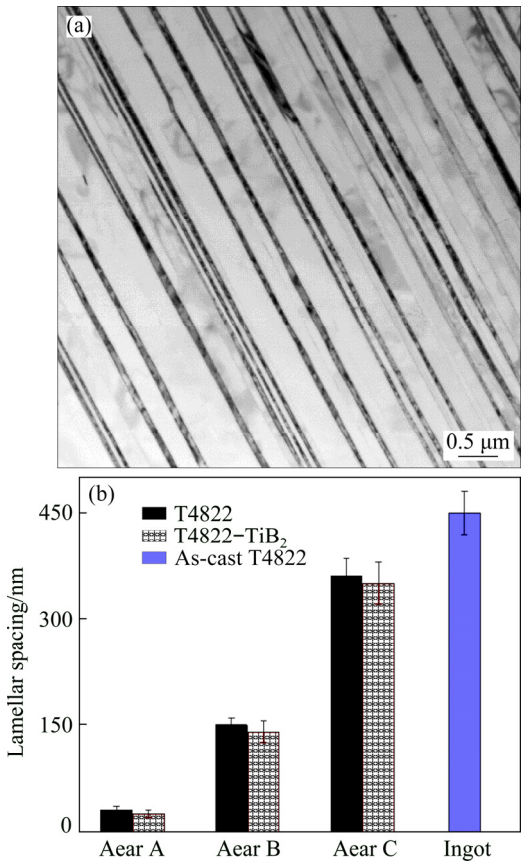

Fig. 8 TEM images of lamellar structure (a) and lamellar spacing statistical results (b) of studied alloys

According to solid-state phase transformation theory of TiAl alloy, the formation of lamellar γ is diffusion-controlled [36]. Therefore, the increase of cooling rate may lead to a large number of α_2/γ, as well as the γ/γ interface, which finally leads to the smaller mean interface spacing. The refined lamellar spacing induced by a fast cooling rate has been found during heat treatment and solidification [37−39]. TANG et al [40] investigated the factors affecting the lamellar spacing in the TiAl alloys with fully lamellar microstructures and found that the lamellar spacing was inversely proportional to the cooling rate. For the fast-cooled TiAl alloy, the lamellar spacing was reported to be less than 35 nm [41], corresponding to the results in the present work.

According to the analysis, the influence of B element on the lamellar spacing appears to be controversial. While in the present study, the TiB_2-containing alloys exhibit slightly refined lamellar spacing than the matrix alloy. According to the analysis of the lamellar transformation in B-containing TiAl alloys [42], refinement of lamellar spacing with trace B addition could be attributed to the solute drag effect of boron atoms on the lateral thickening of γ lamellae. With higher B addition (≥0.2 at.%), the presence of fine boride particles would reduce the supercooling required for lamellar formation, and contribute to the coarse lamellar structure. In the present study, the borides mainly exhibit flaky morphology, which are non-equilibrium morphologies in the view of interfacial energy and strain. The pinning of α grain boundary by such particles will result in the formation of high-energy phase boundary, which contains a high density of defects such as dislocations and planar faults. According to the heterogeneous nucleation theory [43], these boundaries can facilitate the nucleation of γ phase, compared with the normal α/α boundaries. The formation temperature of γ lamellae will be increased by about 50 °C compared with the B-free alloy. With a slow cooling rate, this may result in the coarser lamellar structure. While due to the little wall thickness and grain size, the cooling rates in the present study are larger than those of the conventional ingot manufacturing and heat treatment. This means that the growth time of γ lamellae is insufficient. Therefore, the TiB_2-containing alloy in the present study exhibits the relatively refined lamellar spacing.

3.2 Effect of cooling rate on mechanical properties

Figure 9 shows the microhardness in different areas of the stepped plate casting. It can be seen that, T4822−TiB_2 alloy generally exhibits the higher hardness than the matrix alloy with different cooling rates. However, Area A with the largest cooling rate shows the lowest hardness for the two alloys, while Area B with medium cooling rate exhibits the peak hardness. Area B in T4822−TiB_2 alloy shows the optimal hardness of HV 560, about 17% higher than that of the matrix alloy with the same cooling rate. According to previous research of TiAl alloy, the relationship of microhardness and lamellar spacing can be expressed as [44]

$$H=H_{V0}+k\lambda^{-0.5} \quad (1)$$

where H is microhardness, λ is lamellar spacing,

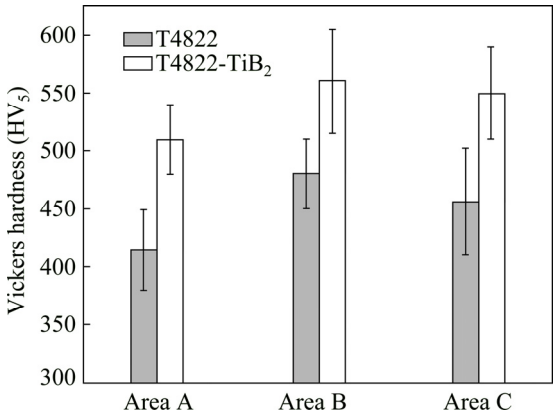

Fig. 9 Microhardnesses of different areas in stepped plate casting

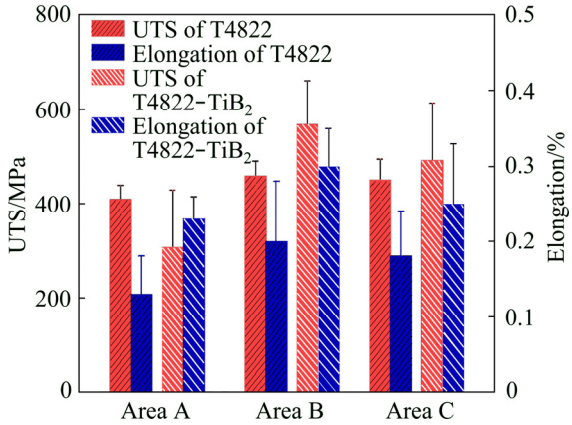

Fig. 10 Room temperature tensile properties of stepped plate casting

H_{V0} and k are constants. Refined lamellar spacing may promote the increase of hardness since the lamellar interface can inhibit the movement of dislocations. In the present work, Area A shows the smallest lamellar spacing than other areas, while there exist a large number of massive γ blocks along the grain boundary. According to the researches of NIU et al [45] and GÖKEN et al [46], the hardness of γ phase in TiAl alloy was 20% lower than that of lamellar structure. Therefore, the effect of fine lamellar spacing appears to be offset by the negative effect of γ particles, resulting in the worst hardness in Area A. With a slower cooling rate, there exist fewer γ particles in Areas B and C, so their hardness and lamellar spacing show the coincident trends. Meanwhile, due to the intrinsic extreme hardness of borides, T4822−TiB_2 alloy exhibits higher hardness than the matrix alloy.

Figure 10 shows the room temperature tensile properties of the stepped plate casting with different cooling rates. It can be seen that the castings with the largest cooling rate (Area A) show the worst tensile properties, corresponding with the hardness results in Fig. 9. The ultimate tensile strength (UTS) of matrix alloy in Area A is 410 MPa, 10% lower than that of Area B, but higher than that of T4822−TiB_2 alloy in Area A (390 MPa). While with a slower cooling rate, T4822−TiB_2 alloy shows the enhanced tensile properties than the matrix alloy. T4822−TiB_2 alloy in Area B exhibits the best tensile property among the stepped plates in the present study, with the UTS of 570 MPa and elongation of 0.3%, which are 24% and 50% higher than those of the matrix alloy, respectively.

For TiAl-based alloy with polycrystalline lamellar microstructure, the tensile strength can be described by the Hall−Petch type function of grain size (d) and lamellar spacing (λ) [47], respectively:

$$\sigma = \sigma_0 + k_d/d^{1/2} + k_\lambda/\lambda^{1/2} \quad (2)$$

where σ_0 is the intrinsic strength of γ phase; k_d and k_λ are material constants. According to this function, the refined grain size and lamellar spacing can promote the strength. This results from the fact that for the fine microstructure, the strain induced by external force can be dispersed in more grains and lamellae, resulting in lower stress concentration. Furthermore, in the study of bimodal titanium alloy with ultrafine lamellar eutectic structure [29,48], the lamellar structure can exhibit phenomenological effects of blocking, branching and multiplying on the high-density dislocations. At the same time, the micro-cracks can also be hindered and restricted by the lamellar eutectic matrix during the plastic deformation. In the present study, fine grain size and lamellar spacing mean more grain boundaries and lamellar interfaces, which can act as obstacles for dislocation slip and enhance the fracture strength reasonably. As discussed above, due to the variation of cooling rate, the grain size and lamellar spacing can be ranged as Area A < Area B < Area C for the studied alloys, while Area B for the two alloys shows the best tensile strength, as shown in Fig. 10. This can be attributed to the massive γ blocks distributing along the grain boundaries. Due to the ordered face-centered tetragonal $L1_0$ structure, the strength and hardness are reported to be lower than those of the lamellar structure. According to the simulation results of shrinkage porosity in Fig. 3 and the SEM images in Fig. 4, the stepped plate castings show few obvious shrinkage porosity

during the centrifugal casting process. However, the serious element segregation in Area A can also affect the physical and chemical uniformity, resulting in the reduction of mechanical properties.

Concerning the higher strength of TiB_2-containing alloy in Area B, the strengthening effect caused by TiB_2 addition can be mainly analyzed from the indirect and direct aspects [49]. The former is the microstructure refinement caused by TiB_2 addition and solid solution of B element, and the latter is the interaction between borides and dislocations. In the view of the low solid solubility of B in α_2 and γ phases, the effect of solid solution strengthening can be basically ignored [50]. Considering the refined microstructure by TiB_2 addition shown in Figs. 6 and 8, this can account for the excellent performance during the tensile test. In addition, the morphology and size of boride also have a great influence on tensile properties. According to the research of HU [7], the UTS of TiAl alloy can be effectively enhanced by finer borides with the same grain size. This is mainly because large boride particles may become the crack source and promote the crack propagation during tensile deformation, and thus deteriorate the mechanical behavior. Compared with the coarse boride in Area C, the fine boride of T4822−TiB_2 alloy in the Area B appears to be helpful for the strength improvement.

Figure 11 shows the morphologies of tensile

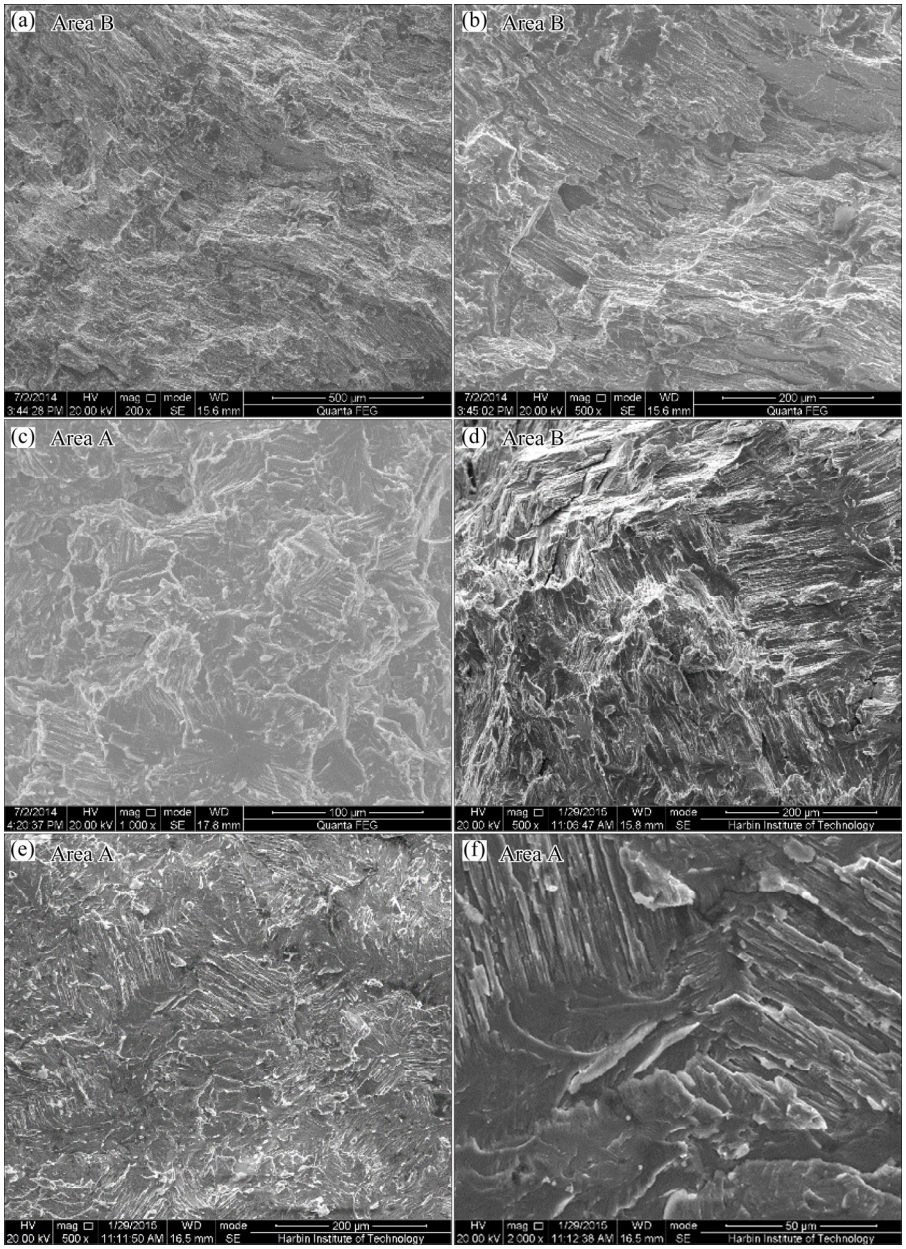

Fig. 11 Morphologies of tensile fracture surface of stepped plates of T4822 (a−c) and T4822−TiB_2 (d−f) alloys

fracture surface of T4822 and T4822−TiB_2 stepped plates. The typical brittle fracture features can be observed for T4822 alloy with medium cooling rate (Figs. 11(a, b)), and there exists no secondary crack and obvious shrinkage porosity. For T4822−TiB_2 alloy, Area B with coarse microstructure exhibits the similar translamellar and interlamellar fracture morphology. With the increase of cooling rate, the brittle fracture features maintain for the samples in Area A, and the refined grain and lamellar structure can be clearly observed, corresponding to the above analysis.

4 Conclusions

(1) As the cooling rate increases from 37 to 2×10^2 K/s, the grain size of T4822−TiB_2 is refined from 550 to 80 μm, which is much smaller than that of the matrix alloy. The grain refinement can be mainly attributed to the auxiliary nucleation of α phase by multiphase TiB_2 particles, and the further supercooling induced by the B element and increased cooling rate.

(2) With the increase of cooling rate, the lamellar spacing of T4822 is reduced from 360 to 30 nm. TiB_2 addition exhibits little refinement effect on the lamellar spacing due to the synthetic action of TiB_2 addition and cooling rate.

(3) T4822−TiB_2 sample under medium cooling rate (Area B) exhibits superior microhardness and tensile properties than the matrix alloy with various cooling rates. The refined microstructure and fine TiB_2 particles are responsible for the favorable mechanical properties of the studied TiB_2-containing alloy.

Acknowledgments

This work is supported by the National Natural Science Foundation of China (51904205), Science and Technology Foundation of State Key Laboratory, China (6142909180205), China Postdoctoral Science Foundation (2018M641681), Scientific and Technological Innovation Programs of Higher Education Institutions in Shanxi Province, China (2019L0216), Shanxi Province Science and Technology Major Program, China (20181101008), and Natural Science Foundation of Shanxi Province, China (201801D221346, 201801D221221).

References

[1] KIM Y W, DIMIDUK D M. Progress in the understanding of gamma titanium aluminides [J]. JOM, 1991, 43: 40−47.

[2] YANG Rui. Advances and challenges of TiAl base alloys [J]. Acta Metallurgica Sinica, 2015, 51: 129−147. (in Chinese)

[3] ZHANG Wei, LIU Yong, LIU Bin, LI Hui-zhong, TANG Bei. Deformability and microstructure transformation of PM TiAl alloy prepared by pseudo-HIP technology [J]. Transactions of Nonferrous Metals Society of China, 2010, 20: 547−552.

[4] CHEN Yu-yong, JIA Yi, XIAO Shu-long, TIAN Jing, XU Li-juan. Review of the investment casting of TiAl-based intermetallic alloys [J]. Acta Metallurgica Sinica, 2013, 49: 1281−1285. (in Chinese)

[5] KIM Y W, KIM S L. Advances in gammalloy materials–processes–application technology: Successes, dilemmas, and future [J]. JOM, 2018, 70: 553−560.

[6] HAN Jian-chao, LIU Zhi-dong, JIA Yi, WANG Tao, ZHAO Li-ping, GUO Ji-bao, XIAO Shu-long, CHEN Yu-yong. Effect of TiB_2 addition on microstructure and fluidity of cast TiAl alloy [J]. Vacuum, 2020, 174: 109210.

[7] HU D. Role of boron in TiAl alloy development: A review [J]. Rare Metals, 2015, 35: 1−14.

[8] CHENG T T. The mechanism of grain refinement in TiAl alloys by boron addition—An alternative hypothesis [J]. Intermetallics, 2000, 8: 29−37.

[9] GOSSLAR D, GUNTHER R, HECHT U, HARTIG C, BORMANN R. Grain refinement of TiAl-based alloys: The role of TiB_2 crystallography and growth [J]. Acta Materialia, 2010, 58: 6744−6751.

[10] SRIVASTAVA D, HU D, CHANG I T H, LORETTO M H. The influence of thermal processing route on the microstructure of some TiAl-based alloys [J]. Intermetallics, 1999, 7: 1107−1112.

[11] MAZIASZ P J, LIU C T. Development of ultrafine lamellar structures in two-phase γ-TiAl alloys [J]. Metallurgical and Materials Transactions A, 1998, 29: 105−117.

[12] WU Y, HWANG S K. The effect of yttrium on microstructure and dislocation behavior of elemental powder metallurgy processed TiAl-based intermetallics [J]. Materials Letters, 2004, 58: 2067−2072.

[13] WU Y, HWANG S K. Microstructural refinement and improvement of mechanical properties and oxidation resistance in EPM TiAl-based intermetallics with yttrium addition [J]. Acta Materialia, 2002, 50: 1479−1493.

[14] WANG Jian-ji, YANG Li-li, ZHENG Li-jing, YAN Jie, XIAO Zhi-xia, LI Guo-qiang, ZHANG Hu. Effect of B, Y and cooling rate on the microstructure refinement of Ti−47Al−2Cr−2Nb alloy [J]. Special Casting and Nonferrous Alloys, 2011, 31: 260−263. (in Chinese)

[15] LI Bao-hui, KONG Fan-tao, CHEN Yu-yong. Effect of yttrium addition on microstructures and room temperature tensile properties of Ti−47Al alloy [J]. Journal of Rare Earths, 2006, 24: 352−356.

[16] LI Bao-hui, CHEN Yu-yong, KONG Fan-tao. Effects of yttrium on microstructure and properties of TiAl alloy [J]. Special Casting and Nonferrous Alloys, 2006, 26: 762−765.

(in Chinese)

[17] ZHOU Can-xu, LIU Bin, LIU Yong, QIU Cong-zhang, LI Hui-zhong, HE Yue-hui. Effect of carbon on high temperature compressive and creep properties of beta-stabilized TiAl alloy [J]. Transactions of Nonferrous Metals Society of China, 2017, 27: 2400−2405.

[18] WU Ze-en, HU Rui, ZHANG Tie-bang, ZHANG Fan, KOU Hong-chao, LI Jin-shan. Understanding the role of carbon atoms on microstructure and phase transformation of high Nb containing TiAl alloys [J]. Materials Characterization, 2017, 124: 1−7.

[19] CUI Ning, WANG Xiao-peng, KONG Fan-tao, CHEN Yu-yong, ZHOU Hai-tao. Microstructure and properties of a beta-solidifying TiAl-based alloy with different refiners [J]. Rare Metals, 2016, 35: 42−47.

[20] JIA Yi, XIAO Shu-long, TIAN Jing, XU Li-juan, CHEN Yu-yong. Modeling of TiAl alloy grating by investment casting [J]. Metals, 2015, 5: 2328−2339.

[21] GAO Yong, ZHANG Li-jing, GAO Wen-li, ZHANG Hu. Prediction and improvement of shrinkage porosity in TiAl based alloy [J]. China Foundry, 2011, 8: 19−24. (in Chinese)

[22] LIU Yi, HU Rui, ZHANG Tie-bang, KOU Hong-chao, WANG Jun, YANG Guang, LI Jin-shan. Dendritic growth and microstructure evolution with different cooling rates in Ti48Al2Cr2Nb alloy [J]. Journal of Materials Engineering and Performance, 2015, 25: 38−45.

[23] YANG L, CHAI L H, LIANG Y F, ZHANG Y W, BAO C L, LIU S B, LIN J P. Numerical simulation and experimental verification of gravity and centrifugal investment casting low pressure turbine blades for high Nb−TiAl alloy [J]. Intermetallics, 2015, 66: 149−155.

[24] ZHANG Y, WANG X P, KONG F T, SUN L L, CHEN Y Y. Microstructure, texture and mechanical properties of Ti−43Al−9V−0.2Y alloy hot-rolled at various temperatures [J]. Journal of Alloys and Compounds, 2019, 777: 795−805.

[25] SCHUSTER J C, PALM M. Reassessment of the binary aluminum−titanium phase diagram [J]. Journal of Phase Equilibria and Diffusion, 2006, 27: 255−277.

[26] HAN J C, XIAO S L, TIAN J, CHEN Y Y, XU L J, WANG X P, JIA Y, DU Z X, CAO S Z. Grain refinement by trace TiB_2 addition in conventional cast TiAl-based alloy [J]. Materials Characterization, 2015, 106: 112−122.

[27] WITUSIEWICZ V T, BONDAR A A, HECHT U, REX S, VELIKANOVA T Y. The Al−B−Nb−Ti system III. Thermodynamic re-evaluation of the constituent binary system Al−Ti [J]. Journal of Alloys and Compounds, 2008, 465: 64−77.

[28] WITUSIEWICZ V T, BONDAR A A, HECHT U, ZOLLINGER J, ARTYUKH L V, VELIKANOVA T Y. The Al−B−Nb−Ti system V: Thermodynamic description of the ternary system Al−B−Ti [J]. Journal of Alloys and Compounds, 2009, 474: 86−104.

[29] YANG C, KANG L M, LI X X, ZHANG W W, ZHANG D T, FU Z Q, LI Y Y, ZHANG L C, LAVERNIA E J. Bimodal titanium alloys with ultrafine lamellar eutectic structure fabricated by semi-solid sintering [J]. Acta Materialia, 2017, 132: 491−502.

[30] KANG L M, YANG C, WANG F, LI X X, ZHU D Z, ZHANG W W, CHEN W P, HUAN Y. Designing ultrafine lamellar eutectic structure in bimodal titanium alloys by semi-solid sintering [J]. Journal of Alloys and Compounds, 2017, 702: 51−59.

[31] ZHANG Li, SU Yan-qing, YANG Hui-min, LUO Liang-shun, GUO Jing-jie. As-cast structure refinement of Ti−46Al alloy by hafnium and boron additions [J]. China Foundry, 2009, 6: 115−118. (in Chinese)

[32] CLEMENS H, MAYER S. Intermetallic titanium aluminides in aerospace applications-processing, microstructure and properties [J]. Materials at High Temperatures, 2016, 33: 560−570.

[33] TILLER W A, JACKSON K A, RUTTER J W, CHALMERS B. The redistribution of solute atoms during the solidification of metals [J]. Acta Metallurgica, 1953, 1: 428−437.

[34] HAN J C, XIAO S L, TIAN J, CHEN Y Y, XU L J, WANG X P, JIA Y, RAHOMA H K S, DU Z X, CAO S Z. Microstructure characterization, mechanical properties and toughening mechanism of TiB_2-containing conventional cast TiAl-based alloy [J]. Materials Science and Engineering A, 2015, 645: 8−19.

[35] GODFREY A B, LORETTO M H. The nature of complex precipitates associated with the addition of boron to a γ-based titanium aluminide [J]. Intermetallics, 1996, 4: 47−53.

[36] BESCHLIESSER M, CHATTERJEE A, LORICH A, KNABL W, KESTLER H, DEHM G, CLEMENS H. Designed fully lamellar microstructures in a γ-TiAl based alloy: Adjustment and microstructural changes upon long-term isothermal exposure at 700 and 800 °C [J]. Materials Science and Engineering A, 2002, 329−331: 124−129.

[37] QIANG F M, KOU H C, TANG B, SONG L, LI J S. Effect of cooling rate on microstructure evolution of Ti−45Al−8.5Nb−0.2W−0.2B−0.02Y alloy during multi-step heat treatment [J]. Materials Characterization, 2018, 145: 210−217.

[38] XU H, LI X B, XING W W, SHU L, MA Y C, LIU K. Phase transformation behavior of a Mn containing beta-solidifying gamma-TiAl alloy during continuous cooling [J]. Intermetallics, 2018, 99: 51−58.

[39] WANG Q, CHEN R R, YANG Y H, WU S P, GUO J J, DING H S, SU Y Q, FU H Z. Effects of lamellar spacing on microstructural stability and creep properties in beta-solidifying gamma-TiAl alloy by directional solidification [J]. Materials Science and Engineering A, 2018, 711: 508−514.

[40] TANG Jian-cheng, HUANG Bai-yun, ZHOU Ke-chao, LIU Wen-sheng, HE Yue-hui, LIU Yong. Factors affecting the lamellar spacing in two-phase TiAl alloys with fully lamellar microstructures [J]. Materials Research Bulletin, 2001, 36: 1737−1742.

[41] PALOMARES-GARCIA A J, SABIROV I, PEREZ-PRADO M T, MOLINA-ALDAREGUIA J M. Effect of nanoscale thick lamellae on the micromechanical response of a TiAl alloy [J]. Scripta Materialia, 2017, 139: 17−21.

[42] ZHANG W J, DEEVI S C. An analysis of the lamellar transformation in TiAl alloys containing boron [J]. Materials Science and Engineering A, 2002, 337: 17−20.

[43] CAHN R W, HAASEM P. Physical metallurgy [M]. 4th ed. Amsterdam: North-Holland Publishing Company, 1996.
[44] FAN Jiang-lei, LI Xin-zhong, SU Yan-qing, GUO Jing-jie, FU Heng-zhi. The microstructure parameters and microhardness of directionally solidified Ti−43Al−3Si alloy [J]. Journal of Alloys and Compounds, 2010, 506: 593−599.
[45] NIU H Z, CHEN Y Y, XIAO S L, XU L J. Microstructure evolution and mechanical properties of a novel beta γ-TiAl alloy [J]. Intermetallics, 2012, 31: 225−231.
[46] GÖKEN M, KEMPF M, NIX W D. Hardness and modulus of the lamellar microstructure in PST-TiAl studied by nanoindentations and AFM [J]. Acta Materialia, 2001, 49: 903−911.
[47] DIMIDUK D M, HAZZLEDINE P M, PARTHASARATHY T A, MENDIRATTA M G, SESHAGIRI S. The role of grain size and selected microstructural parameters in strengthening fully lamellar TiAl alloys [J]. Metallurgical and Materials Transactions A, 1998, 29: 37−47.
[48] KANG Li-mei, YANG Chao. A review on high-strength titanium alloys: Microstructure, strengthening, and properties [J]. Advanced Engineering Materials, 2019, 21: 1801359.
[49] KAMPE S L, SADLER P, CHRISTODOULOU L, LARSEN D E. Room-temperature strength and deformation of TiB_2-reinforced near-γ titanium aluminides [J]. Metallurgical And Materials Transactions A, 1994, 25: 2181−2197.
[50] NIU H Z, XIAO S L, KONG F T, ZHANG C J, CHEN Y Y. Microstructure characterization and mechanical properties of TiB_2/TiAl in situ composite by induction skull melting process [J]. Materials Science and Engineering A, 2012, 532: 522−527.

冷却速率对含 TiB_2 的 TiAl 合金凝固组织和力学性能的影响

贾 崴[1,2,3]，刘志栋[1]，李 莎[1,2,3]，姚昊明[1,2,3]，任忠凯[1,2,3]，
王 涛[4]，韩建超[1,2,3]，肖树龙[4]，陈玉勇[4]

1. 太原理工大学 机械与运载工程学院，太原 030024；
2. 太原理工大学 先进金属复合材料成形技术与装备教育部工程研究中心，太原 030024；
3. 太原理工大学 TYUT-UOW 联合研究中心，太原 030024；
4. 哈尔滨工业大学 金属精密热加工国防重点实验室，哈尔滨 150001

摘 要：通过熔模精密铸造制备不同厚度的 Ti−48Al−2Cr−2Nb 和 Ti−48Al−2Cr−2Nb−0.25TiB_2 合金铸板，研究冷却速率和 TiB_2 添加对合金凝固组织和力学性能的影响。实验结果表明，当凝固速率从 37 增加至 2×10^2 K/s 时，合金的凝固路径并未发生改变。基体合金的晶粒从 650 细化至 300 μm，Ti−48Al−2Cr−2Nb−TiB_2 合金的晶粒则从 550 细化至 80 μm。随着冷却速率从 37 提高至 2×10^2 K/s，基体合金的片层间距从 360 减小至 30 nm，TiB_2 添加对片层间距的影响较小。在中等冷却速率下(69 K/s)，Ti−48Al−2Cr−2Nb−TiB_2 合金铸板表现出最优的力学性能，显微硬度达到 HV 550，极限抗拉强度达到 570 MPa，这主要归因于晶粒尺寸、片层间距的细化和细小 TiB_2 颗粒的作用。从冷却速率、成分过冷和添加硼化物等角度对显微组织演化过程进行详细讨论。

关键词：TiAl 合金；TiB_2；冷却速率；显微组织演化；力学性能

(Edited by Bing YANG)